communications biology

A Nature Portfolio journal

Article

https://doi.org/10.1038/s42003-026-09518-w

MAT2A enhances *PARN* transcription via SRF to accelerate glycolysis and drive malignant progression in osteosarcoma

Zhinan Ren[1,8], Haoming Chen[2,3,4,5,8], Qi Qiao[6,8], Zehao Xie[2,3,4], Jianhua Hu[2,3,4], Canjun Zeng[2,3,4] ✉, Yi Shen[7] ✉ & Runguang Li[2,3,4] ✉

Osteosarcoma lacks effective molecular targets, and the biological role of MAT2A in this disease remains unclear. Here we show that MAT2A drives osteosarcoma progression by increasing the transcription of the downstream gene *PARN*. MAT2A interacts with the transcription factor SRF, promotes its SUMO-dependent stabilization in the nucleus, and enhances its ability to activate PARN. A catalytically inactive MAT2A mutant retains this function, indicating a SAM-independent mechanism. MAT2A also elevates aerobic glycolysis in osteosarcoma cells through the PARN–PI3K–AKT pathway, while pharmacological inhibition of MAT2A reduces glycolysis, SRF and PARN expression, and tumor growth in vitro and in vivo. These findings identify a previously unrecognized regulatory mechanism linking MAT2A to transcriptional control and metabolic reprogramming, and highlight MAT2A as a promising therapeutic target for osteosarcoma.

Osteosarcoma (OS) is the most common primary malignant tumor of bone, originating from osteoblasts, and it usually affects children and adolescents. It accounts for approximately 20% of all primary malignant bone tumors worldwide[1]. Metastasis of the primary tumor remains the leading cause of mortality in patients with OS[2]. Owing to advancements in surgical techniques, effective chemotherapeutic agents, and both preoperative and postoperative chemoradiotherapy, the overall survival rate has improved significantly in recent decades[3]. Nevertheless, the treatment of OS has reached a major bottleneck, particularly for patients with metastasis, recurrence, or chemotherapy resistance[4]. Managing these patients requires the development of new and effective molecular targets, drugs, and innovative therapeutic strategies. Research on oncogenes and tumor suppressors has gained considerable momentum. Targeted therapies and optimal combinations of different treatment modalities are expected to provide new opportunities for OS management[5]. However, only a few therapeutic targets have demonstrated satisfactory clinical performance. Thus, it is imperative to identify novel molecular targets for OS treatment.

Mammals contain three distinct forms of methionine adenosyltransferase (MAT)—MATI, MATII, and MATIII—encoded by two genes, *MAT1A* and *MAT2A*. MATII is composed of the α2 catalytic subunit encoded by *MAT2A* and the β regulatory subunit encoded by *MAT2B*[6,7]. The metabolic enzyme methionine adenosyltransferase 2 alpha (MAT2A) is a key regulator of cellular metabolism and is primarily responsible for catalyzing the conversion of L-methionine and adenosine triphosphate (ATP) into S-adenosylmethionine (SAM)[8]. SAM serves as the principal methyl donor for most methyltransferases and is essential for the DNA, RNA, and protein methylation processes required for diverse cellular functions[9].

Accumulating evidence has shown that MAT2A is overexpressed in various tumors, including hepatic cancer[10,11], breast cancer[12], gastric cancer[13], lung cancer[14] and glioma[15]. Importantly, MAT2A plays a critical role in cancer progression and is considered a promising therapeutic target. For example, Yang et al. reported that the MAT2A regulatory pathway is essential for cisplatin-resistant bladder cancer cells[16]. Wang et al. demonstrated that high MAT2A expression is associated with poor prognosis in patients with recurrent multiple myeloma and that the MAT2A inhibitor FIDAS-5 enhances the therapeutic efficacy of bortezomib-based treatment[17]. Moreover, Xia et al. showed that MAT2A suppresses ferroptosis during OS progression through regulation by miR-26b-5p[18]. Despite

[1]Department of Orthopedics, the First Affiliated Hospital of Zhengzhou University, Henan Province, Zhengzhou, China. [2]Department of Foot and Ankle Surgery, Center for Orthopaedic Surgery, the Third Affiliated Hospital of Southern Medical University, Guangdong Province Guangzhou, China. [3]Orthopaedic Hospital of Guangdong Province, Guangzhou, China. [4]Academy of Orthopaedics, Guangdong Province Guangzhou, China. [5]Division of Spine Surgery, Department of Orthopaedics, Nanfang Hospital, Southern Medical University, Guangdong Province Guangzhou, China. [6]Department of Geriatric Endocrinology, the First Affiliated Hospital of Zhengzhou University, Henan Province, Zhengzhou, China. [7]Department of Orthopaedics, The Second Xiangya Hospital of Central South University, Hunan Province, Changsha, China. [8]These authors contributed equally: Zhinan Ren, Haoming Chen, Qi Qiao. ✉e-mail: zengcanjun@163.com; shenyiak487@163.com; lrg1979@smu.edu.cn

these findings, the mechanistic role of MAT2A in osteosarcoma remains incompletely understood and warrants further investigation.

In our study, we first analyzed the expression level of MAT2A in OS and its association with clinicopathological characteristics. We then investigated the biological functions of MAT2A in OS through both in vitro and in vivo experiments. More importantly, we explored the potential molecular mechanism by which MAT2A regulates OS progression and examined whether pharmacological inhibition of MAT2A could offer a novel therapeutic avenue for OS. Altogether, our findings expand the understanding of MAT2A in OS and suggest that it may serve as a promising therapeutic target for OS treatment.

Results

High MAT2A expression correlates with osteosarcoma progression

We performed bioinformatic analysis on single-cell RNA sequencing (scRNA-seq) data, integrating samples using the anchor-based method to remove batch effects. After standardization, dimensionality reduction, and clustering, we identified 23 distinct cell clusters visualized by UMAP (Fig. 1A). Cell-type annotation revealed eight major populations, including myeloid cells, osteoblastic cells, T cells, NKT cells, fibroblasts, B cells, endothelial cells, and other unclassified cell types (Fig. 1B). Comparative analysis showed that fibroblasts and osteoblastic cells were enriched in OS, whereas myeloid and B cells were depleted (Fig. 1C, D), indicating tumor-associated alterations in cellular composition.

Gene expression analyses demonstrated significant transcriptional differences between OS and normal tissues. The dot plot (Fig. 1E) showed increased expression of tumor-associated genes and reduced expression of immune-related genes in OS. Differential expression analysis further identified key dysregulated genes, as shown in the volcano plot and heatmap (Fig. 1F, G), highlighting multiple genes with substantial expression changes in OS. Among these, *MAT2A* exhibited marked upregulation, reinforcing its potential role in tumor progression.

Analysis of TCGA datasets further demonstrated aberrant *MAT2A* expression across multiple cancer types (Supplementary Fig. 1A). Consistently, independent validation using the GEO dataset (GSE16088) confirmed that *MAT2A* expression was significantly elevated in OS compared with normal tissues (Fig. 1H). To further examine the endogenous expression of MAT2A in OS, we performed immunohistochemical (IHC) staining on a tissue microarray. The results showed a progressive increase in MAT2A-positive staining from normal tissues to advanced OS tissues. For quantitative evaluation, samples were classified into high- and low-expression groups based on the median staining intensity. Statistical analysis confirmed that MAT2A expression was significantly elevated in OS tissues compared with normal controls (Fig. 1I, Supplementary Table 1).

Consistently, MAT2A expression in OS cell lines was markedly higher than in osteoblasts (hfOB 1.19), particularly in MNNG/HOS and U-2OS cells (Fig. 1J, K). Furthermore, leveraging clinical data from OS patients, we conducted statistical analyses to assess the correlation between MAT2A expression and pathological characteristics. Our results demonstrated a significant positive correlation between MAT2A expression and both disease stage and lymphatic metastasis (Supplementary Table 2). Collectively, these findings highlight the abnormally elevated expression of MAT2A in

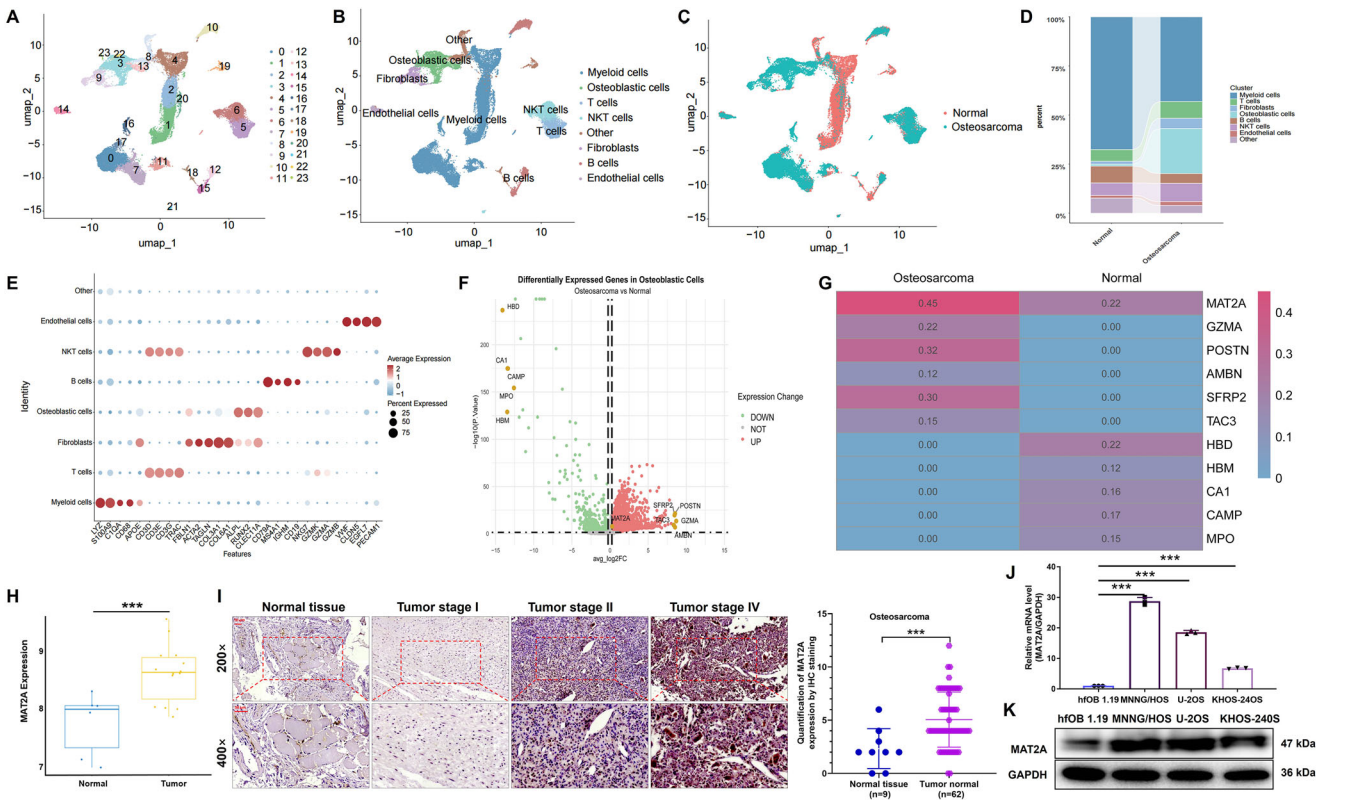

Fig. 1 | High MAT2A expression correlates with osteosarcoma progression. **A** UMAP plot showing the clustering of single-cell samples into 23 distinct clusters. **B** Identification of eight cell types based on the expression of specific marker genes. **C** UMAP clustering plot comparing normal and OS tissues. **D** Proportional representation of the different cell types across the samples. **E** Dot plot illustrating the expression of selected marker genes for each identified cell type. **F** Volcano plot showing differential gene expression, highlighting significant differences. **G** Gene heatmap showing differential gene expression, highlighting significant differences. **H** Expression of *MAT2A* in OS tissue and normal tissue as shown in GSE 16088 database. **I** MAT2A endogenous expression was determined in normal tissues and OS tissues with different tumor stage (scale bar = 50 μm) and quantitative analysis results of MAT2A in OS tissue and normal tissue ($n = 71$ patients). **J**, **K** Expression of MAT2A in OS cells and osteoblasts was analyzed by (**J**) qRT-PCR and (**K**) WB ($n = 3$ independent experiments). GAPDH was used as the reference gene and loading control. Results were presented as mean ± SD. $^{***}P < 0.001$.

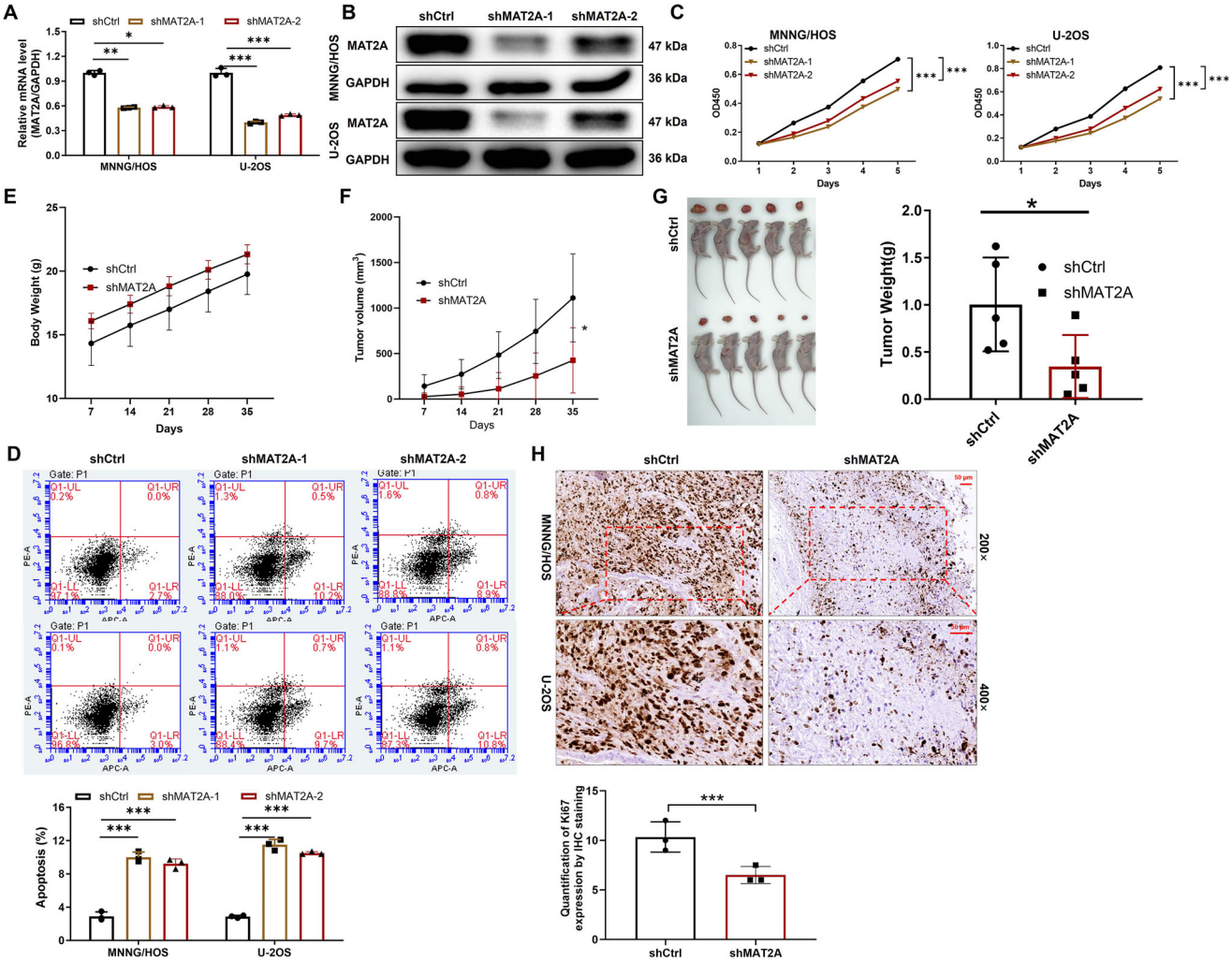

Fig. 2 | MAT2A is essential for the proliferation and tumorigenic ability of OS cells. A Quantitative real-time PCR analysis of *MAT2A* mRNA expression in OS cells (MNNG/HOS and U-2OS) transfected with shCtrl, shMAT2A-1, or shMAT2A-2. **B** Western blot validation of MAT2A protein expression in MNNG/HOS and U-2OS cells after stable knockdown; GAPDH served as the loading control. **C** Cell proliferation curves determined by CCK-8 assay showing significantly reduced growth in MAT2A-depleted OS cells compared with shCtrl cells. **D** Flow cytometric analysis of apoptosis in MNNG/HOS and U-2OS cells with MAT2A knockdown, and quantitative comparison of apoptotic cell percentages. **E** Body weight changes of tumor-bearing mice injected subcutaneously with MNNG/HOS cells stably expressing shCtrl or shMAT2A ($n = 5$ per group). **F** Tumor growth curves showing suppressed tumor volume in the shMAT2A group compared with shCtrl. **G** Representative images of xenograft tumors and corresponding quantitative analysis of tumor weight. **H** Representative IHC staining of Ki-67 in tumor sections from mice injected with shCtrl or shMAT2A MNNG/HOS cells (scale bar = 50 μm) and quantification of Ki-67-positive cells. Data are presented as mean ± SD from three independent experiments. *i < 0.05, **$P < 0.01$, **$P < 0.001$.

OS and suggest a potentially crucial role for MAT2A in osteosarcoma pathogenesis.

Knockdown of MAT2A inhibits proliferation and tumorigenesis of OS cells

To investigate the functional significance of MAT2A in OS cells, we transfected MNNG/HOS and U-2OS cells with shRNA sequences specifically targeting *MAT2A* (Supplementary Fig. 1B). The efficiency of MAT2A knockdown was subsequently validated using qRT-PCR and Western blotting, confirming the successful establishment of *MAT2A*-silenced cell lines (Fig. 2A, B). In these knockdown models, OS cells with reduced MAT2A expression (shMAT2A) exhibited a significantly lower proliferation rate compared with the shCtrl group (Fig. 2C). Consistently, MAT2A-silenced MNNG/HOS and U-2OS cells showed a higher proportion of apoptotic cells than shCtrl cells (Fig. 2D).

In vivo, subcutaneous xenograft models were established by injecting MNNG/HOS cells with or without MAT2A knockdown. As shown, there was no significant difference in the body weight of mice (Fig. 2E), whereas MAT2A silencing markedly inhibited tumor growth (Fig. 2F). After the mice were sacrificed and tumors were excised, those derived from shMAT2A-transfected cells were significantly smaller than those from control cells (Fig. 2G). Consistently, compared with shCtrl tumor tissues, MAT2A deficiency resulted in reduced Ki-67 expression and lower proliferative activity (Fig. 2H). Collectively, these data demonstrate that MAT2A knockdown suppresses the proliferation and tumorigenic potential of OS cells.

Knockdown of MAT2A suppresses aerobic glycolysis in OS cells

An analysis based on the Kyoto Encyclopedia of Genes and Genomes (KEGG) revealed that *MAT2A* knockdown resulted in a significant enrichment of the PI3K/AKT signaling pathway (Fig. 3A). Furthermore, when MAT2A-overexpressing OS cells were treated with the PI3K/AKT pathway inhibitor LY294002, their proliferation, apoptosis, and the expression of key pathway components were markedly altered (Fig. 3B, D).

Given that activation of the phospho-PI3K/AKT signaling pathway has been reported to enhance aerobic glycolysis and

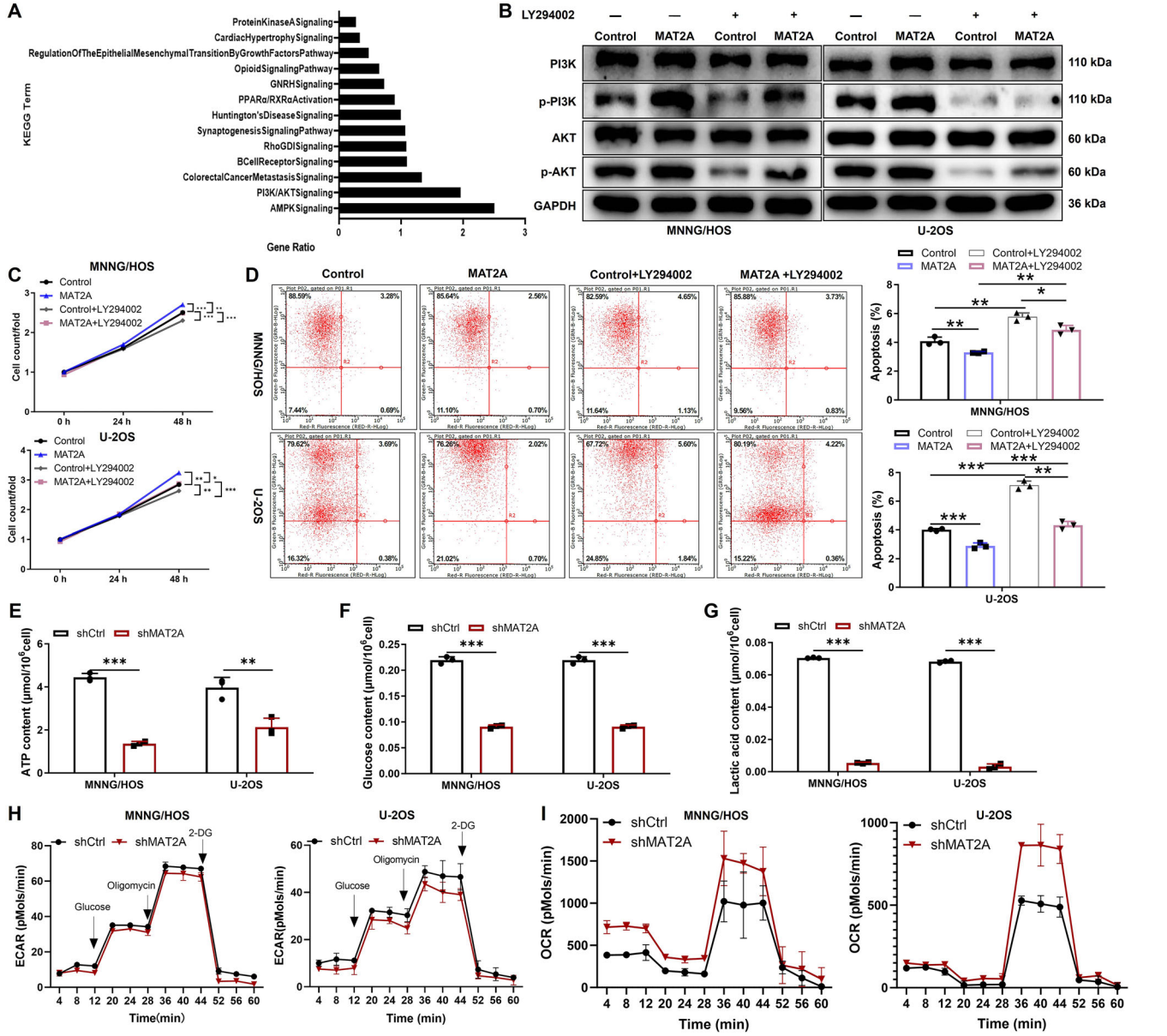

Fig. 3 | MAT2A knockdown inhibits aerobic glycolysis in OS. A The potential mechanism of MAT2A in OS cells was analyzed by KEGG enrichment analysis. The names of enrichment pathways are shown on the left axis. The abscissa is enrichment factor. The high enrichment factor indicates that the enrichment of different proteins in this pathway is significant. **B** The effect of MAT2A overexpression on typical components in the PI3K/AKT signaling pathway was detected by WB. **C**, **D** The effects of MAT2A overexpression and LY294002 treatment (PI3K inhibitor) on MNNG/HOS and U-2OS cells proliferation and apoptosis were detected. **E** ATP level, (**F**) glucose uptake, (**G**) lactic acid production, (**H**) ECAR and (**I**) OCR were detected in MAT2A knockdown and control OS cells. Data are presented as mean ± SD from three independent experiments. $^{**}P < 0.01$, $^{**}P < 0.001$.

promote the malignant progression of OS[19], we next sought to determine whether MAT2A modulates aerobic glycolysis in OS cells. To this end, MAT2A knockdown was performed in osteosarcoma cells. This intervention led to substantial decreases in ATP, glucose, and lactic acid levels. In addition, we observed a reduction in the extracellular acidification rate (ECAR) and a concomitant increase in the oxygen consumption rate (OCR) (Fig. 3E, I). Collectively, these findings indicate that MAT2A knockdown significantly suppresses aerobic glycolysis in OS cells.

MAT2A promotes SRF-mediated transcription of *PARN*

To elucidate the molecular mechanisms through which MAT2A regulates OS progression, we performed GeneChip microarray analysis to identify genes transcriptionally modulated by MAT2A. Under stringent criteria (|Fold Change| ≥ 1.3 and FDR < 0.05), 737 upregulated genes and 1627 downregulated genes were identified (Supplementary Fig. 1C, Fig. 4A). Using rigorous filtering, we further narrowed the candidates to the top ten most promising genes, which were subsequently validated by qRT-PCR (Fig. 4B) and Western blotting (Fig. 4C). Notably, MAT2A knockdown in OS cells resulted in a pronounced reduction in *PARN* expression. Analysis of TCGA datasets further revealed aberrant *PARN* expression across multiple cancer types (Supplementary Fig. 1D). Moreover, Pearson correlation analysis showed a significant positive association between *MAT2A* and *PARN* expression levels (Fig. 4D). These findings led us to hypothesize that MAT2A may exert its regulatory effects in OS by modulating *PARN* expression.

Next, using the STRING database, we identified 1577 potential proteins predicted to interact with MAT2A. In parallel, interrogation of the Broad-GTRD database revealed 40 transcription factors predicted to regulate PARN. Intersection of these two datasets yielded three common

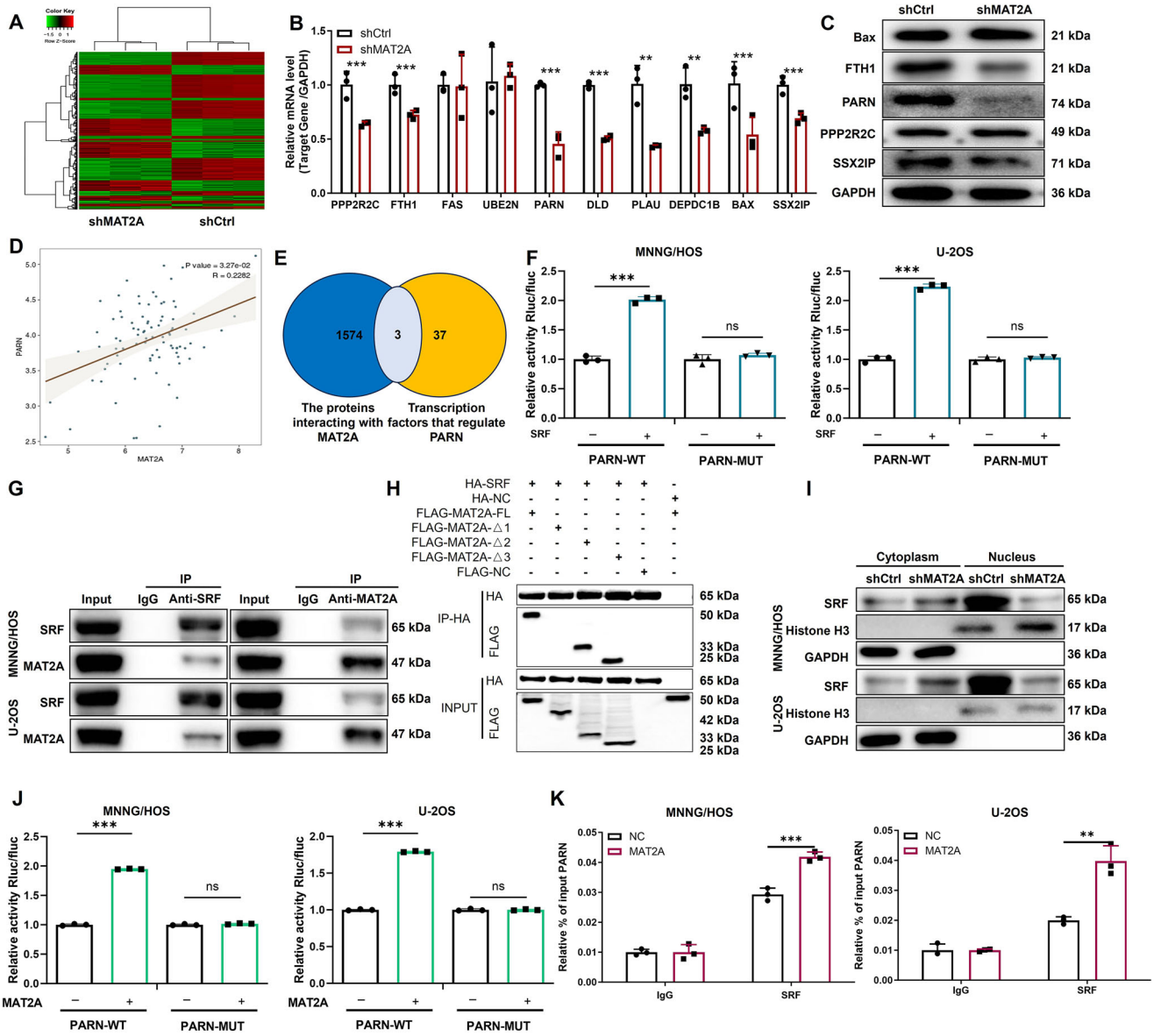

Fig. 4 | MAT2A regulates PARN transcription through interaction with SRF. **A** In the heat map of cluster analysis, each column represented a sample and each row represents a differential gene. The red indicated that the gene expression is upregulated, the green indicated that the gene expression is downregulated, the black indicated that the gene expression is not significantly changed, and the gray indicates that the signal strength of the gene was not detected. **B**, **C** The expression of several most significantly differentially expressed genes was identified by (**B**) qRT-PCR and (**C**) WB. **D** There was a positive correlation between MAT2A and PARN expression. **E** Venn diagram of overlapping transcription factors that both interact with MAT2A and regulate PARN. **F** Dual luciferase reporter gene assays were conducted on luciferase genes harboring both wild-type (*PARN*-WT) and mutated PARN (*PARN*-MUT) promoter regions. **G** CO-IP of MNNG/HOS and U-2OS cell lysates with SRF or MAT2A antibodies revealed the interaction between SRF and MAT2A. **H** Co-IP analysis using full-length MAT2A (MAT2A-FL) and three deletion mutants-Δ1 (deletion of aa 2–70), Δ2 (deletion of aa 71–330), and Δ3 (deletion of aa 331–395)—demonstrating that removal of the N-terminal region (Δ1) abolishes MAT2A–SRF binding, indicating that residues 2–70 are essential for the interaction. **I** Cytoplasmic and nuclear isolation experiments showed that MAT2A knockdown inhibited SRF expression in OS nucleus. **J** Double luciferase reporter gene assay was performed for the luciferase gene in the promoter region of wild type (*PARN*-WT) and mutated PARN (*PARN*-MUT) in MAT2A knockdown and control OS cells. **K** ChIP analysis of SRF binding to the *PARN* promoters in MAT2A overexpression and control OS cells. qRT-PCR was performed with primers specific to the *PARN*-binding motifs. Data were normalized to the input. Data are presented as mean ± SD from three independent experiments. $^{**}P < 0.01$, $^{***}P < 0.001$.

transcription factors, among which SRF demonstrated the strongest predicted interaction with MAT2A (Fig. 4E).

To validate this prediction, we performed dual-luciferase reporter assays using constructs containing either the wild-type (*PARN*-WT) or mutated (*PARN*-MUT) *PARN* promoter regions. As shown in Fig. 4F, SRF robustly increased the luciferase activity of *PARN*-WT but failed to enhance the activity of *PARN*-MUT, indicating that SRF directly binds to the *PARN* promoter. Additionally, co-immunoprecipitation of MNNG/HOS and U-2OS cell lysates using antibodies against SRF or MAT2A revealed the presence of SRF within MAT2A immunoprecipitates, supporting the existence of a protein interaction between MAT2A and the transcription factor SRF (Fig. 4G).

To further delineate the specific structural domain of MAT2A responsible for its association with SRF, we constructed a series of truncation mutants: MAT2A-Δ1 (aa 2–70), MAT2A-Δ2 (aa 71–330), and MAT2A-Δ3 (aa 331–395). Co-immunoprecipitation (CO-IP) analysis revealed that deletion of the N-terminal fragment (aa 2–70) completely abolished MAT2A–SRF binding, whereas the Δ2 and Δ3 mutants retained their

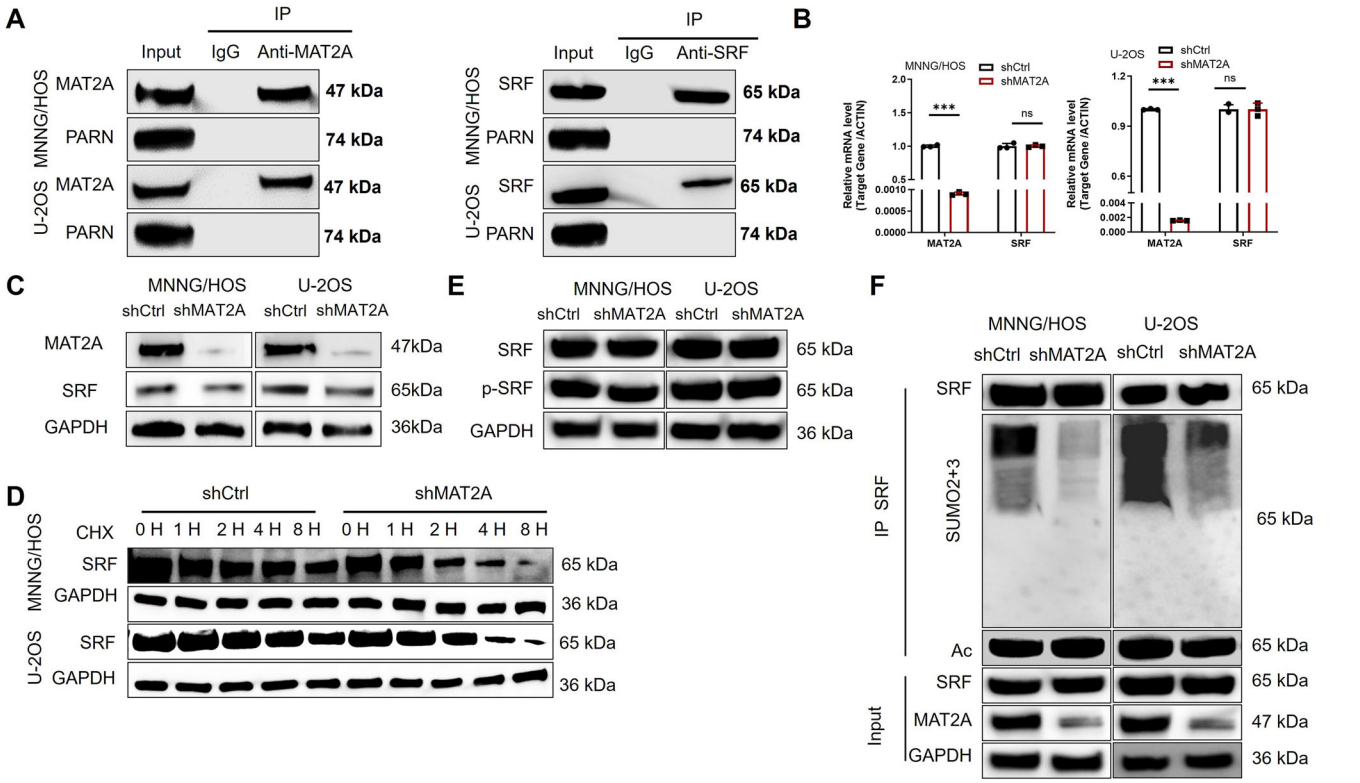

Fig. 5 | MAT2A enhances SUMOylation and stabilization of SRF to facilitate PARN transcription. A Co-IP analysis in MNNG/HOS and U-2OS cells showing that neither MAT2A nor SRF physically interacts with PARN. Immunoprecipitation with anti-MAT2A or anti-SRF antibodies followed by immunoblotting for PARN revealed no detectable interaction, indicating that PARN is not directly associated with MAT2A–SRF complexes. **B** qRT-PCR analysis showing that *MAT2A* knockdown significantly decreased *MAT2A* mRNA expression but had no effect on *SRF* transcript levels in MNNG/HOS and U-2OS cells ($P < 0.001$, ns: not significant). **C** Western blot analysis showing that SRF protein levels were markedly reduced following MAT2A knockdown, while MAT2A loss was confirmed in parallel. GAPDH served as loading control. **D** CHX chase assay demonstrating accelerated degradation of SRF protein in MAT2A-depleted cells compared with control cells, indicating that MAT2A positively regulates SRF protein stability. Cells were treated with CHX (100 μg/mL) and harvested at the indicated time points (0–8 h). **E** Western blot analysis showing that MAT2A knockdown caused no obvious changes in total or phosphorylated SRF (p-SRF) levels, suggesting that MAT2A does not significantly affect SRF phosphorylation status. **F** CO-IP analysis of SRF post-translational modifications in control and MAT2A-knockdown MNNG/HOS and U-2OS cells. MAT2A silencing markedly reduced SUMO2/3-conjugated SRF, while acetylated SRF (Ac-SRF) levels remained unchanged, suggesting that MAT2A specifically promotes SRF SUMOylation. Input controls confirmed equal loading of MAT2A, SRF, and GAPDH. Data are presented as mean ± SD from three independent experiments. $^{*}P < 0.05$, $^{**}P < 0.01$, $^{**}P < 0.001$.

interaction capacity (Fig. 4H). These findings indicate that the N-terminal 2–70 amino acids of MAT2A are indispensable for mediating its interaction with SRF.

Moreover, cytoplasmic–nuclear fractionation assays showed that MAT2A knockdown reduced the nuclear levels of SRF in OS cells (Fig. 4I). Furthermore, MAT2A overexpression significantly increased the luciferase activity driven by the PARN promoter (Fig. 4J). We next performed Chromatin Immunoprecipitation-Quantitative Polymerase Chain Reaction (ChIP–qPCR) targeting conserved PARN promoter regions using IgG or SRF antibodies in MAT2A-overexpressing MNNG/HOS and U-2OS cells, which confirmed that MAT2A enhances *PARN* transcription by promoting SRF binding to its promoter (Fig. 4K). Taken together, these results demonstrate that MAT2A regulates *PARN* expression through SRF.

MAT2A promotes SUMOylation and stabilization of SRF to facilitate *PARN* transcription

To further elucidate how MAT2A enhances SRF-mediated transcription of the downstream target PARN, we explored the post-translational regulation of SRF by MAT2A. Co-IP assays revealed that neither MAT2A nor SRF directly interacts with PARN, indicating that PARN is not physically associated with MAT2A–SRF complexes (Fig. 5A). Interestingly, MAT2A knockdown had no significant effect on the mRNA level of SRF, whereas the SRF protein abundance was markedly reduced (Fig. 5B, C), suggesting that MAT2A may regulate SRF at the post-translational level.

To assess whether MAT2A affects SRF stability, we performed cycloheximide (CHX) chase assays to monitor SRF degradation dynamics. The results showed that MAT2A depletion substantially accelerated SRF degradation, thereby reducing its protein stability (Fig. 5D). These findings indicate that MAT2A positively regulates SRF protein stability.

Given that various post-translational modifications—including phosphorylation, acetylation, and SUMOylation—have been reported to modulate SRF activity and stability[20–22], we next investigated which of these modifications might be influenced by MAT2A. Western blot analysis demonstrated that MAT2A knockdown had minimal impact on SRF phosphorylation and acetylation but caused a pronounced reduction in SRF SUMOylation (Fig. 5E, F). Considering the established role of SUMO modification in maintaining protein stability and oncogenic activation[23,24], these results suggest that MAT2A enhances SRF SUMOylation to stabilize SRF.

In addition, we investigated whether the catalytic activity of MAT2A—the enzyme responsible for synthesizing SAM—is required for the regulation of the SRF–PARN axis. To this end, we constructed a catalytically inactive mutant MAT2A (D180A) and compared its function with that of the wild-type protein. Interestingly, the D180A mutant exhibited a similar capacity to promote SRF nuclear localization and PARN expression as the wild-type MAT2A (Supplementary Fig. 2A, B), suggesting that the enzymatic activity of MAT2A is dispensable for this regulatory process.

Collectively, our findings demonstrate that MAT2A promotes SRF SUMOylation, thereby increasing its protein stability and nuclear retention, which in turn enhances SRF-dependent transcriptional activation of PARN. This post-translational regulatory mechanism, independent of MAT2A's catalytic activity, provides a novel layer of control within the MAT2A–SRF–PARN axis in osteosarcoma cells.

MAT2A facilitates proliferation and migration of OS cells through PARN

To elucidate the mechanism by which MAT2A regulates OS progression, we manipulated the expression of MAT2A or PARN in OS cells. Loss- and gain-of-function experiments demonstrated that PARN knockdown attenuated the MAT2A-induced promotion of proliferation and migration, while reversing its inhibitory effect on apoptosis in MAT2A-overexpressing OS cells (Fig. 6A–C). Conversely, PARN overexpression partially counteracted the phenotypic changes induced by MAT2A knockdown (Supplementary Fig. 3A–F). Collectively, these findings indicate that MAT2A drives OS cell progression through PARN.

MAT2A enhances aerobic glycolysis of OS through PARN–AKT signaling

To further investigate whether MAT2A regulates glycolysis in osteosarcoma (OS) cells via PARN-mediated signaling, we performed a series of rescue experiments. Western blot analysis demonstrated that overexpression of PARN largely restored the phosphorylation levels of PI3K and AKT suppressed by MAT2A knockdown (Fig. 7A), suggesting that MAT2A modulates the PI3K/AKT signaling pathway in a PARN-dependent manner. Consistently, PARN overexpression also reversed the effects of MAT2A depletion on the expression of key glycolytic enzymes, including PKM2 and ADH4 (Fig. 7B).

Functionally, PARN knockdown significantly attenuated MAT2A-induced increases in ATP production, glucose uptake, and lactate generation, while MAT2A overexpression rescued these metabolic reductions (Fig. 7C–E). Seahorse flux analysis further confirmed that PARN silencing abrogated the MAT2A-induced elevation of the ECAR and reduction in the OCR, both of which were restored by PARN re-expression (Fig. 7F–G). Collectively, these findings indicate that the pro-glycolytic role of MAT2A in OS is dependent on PARN.

To further clarify whether this metabolic regulation is mediated through the downstream AKT pathway, we introduced a constitutively active form of AKT (myr-AKT) into MAT2A-depleted OS cells. As shown in Fig. 7H, reintroduction of myr-AKT markedly increased p-AKT levels but had no significant effect on MAT2A, SRF, or PARN expression, confirming the specificity of this manipulation. Functionally, AKT reactivation effectively reversed the metabolic phenotypes induced by MAT2A knockdown, including the reduced lactate production (Fig. 7I), decreased ECAR (Fig. 7J), and elevated OCR (Fig. 7K).

Together, these data demonstrate that MAT2A promotes aerobic glycolysis in osteosarcoma through PARN-dependent activation of the PI3K/AKT signaling pathway, thereby enhancing cellular energy metabolism and supporting tumor progression.

MAT2A-driven aerobic glycolysis participates in OS tumorigenesis through PARN

To verify that MAT2A promotes tumorigenesis by enhancing aerobic glycolysis, we performed xenograft experiments using OS cells with PARN knockdown or MAT2A overexpression. Notably, mice implanted with MAT2A-overexpressing cells developed larger tumors than those implanted with control cells, whereas the tumorigenic potential was markedly impaired when PARN was silenced (Fig. 8A–B), with no significant difference in body weight among groups (Fig. 8C). Furthermore, tumors derived from PARN-knockdown cells exhibited reduced expression of the proliferative marker Ki-67, whereas MAT2A overexpression produced the opposite effect (Fig. 8D). In addition, the expression of key glycolytic proteins was upregulated in tumors formed by MAT2A-overexpressing cells but significantly suppressed in those derived from PARN-knockdown cells. Importantly, the glycolytic upregulation induced by MAT2A overexpression was abolished by concomitant PARN knockdown (Fig. 8E).

Collectively, these findings demonstrate that MAT2A overexpression promotes OS tumor formation by enhancing PARN-dependent aerobic glycolysis.

Pharmacological inhibition of MAT2A suppresses osteosarcoma progression in vitro and in vivo

To further evaluate the therapeutic potential of targeting MAT2A in OS, we examined the effects of the specific MAT2A inhibitor FIDAS-5 on SRF/PARN signaling and tumor progression. Subcellular fractionation analysis revealed that FIDAS-5 treatment markedly reduced nuclear accumulation of SRF in a dose-dependent manner (Fig. 9A). Consistently, western blot analysis showed that FIDAS-5 dose-dependently decreased the phosphorylation levels of PI3K and AKT, confirming inhibition of the PI3K/AKT signaling pathway (Fig. 9B).

Functionally, FIDAS-5 significantly suppressed aerobic glycolysis in OS cells. Consistently, FIDAS-5 treatment markedly reduced lactate production in both MNNG/HOS and U-2OS cells (Fig. 9C). Seahorse assay results further showed that FIDAS-5 induced a dose-dependent decrease in the ECAR and a concomitant increase in the OCR, indicating both impaired glycolytic flux and enhanced mitochondrial respiration (Fig. 9D–E).

Consistent with these metabolic effects, FIDAS-5 significantly inhibited OS cell proliferation in a time- and dose-dependent manner, as evidenced by CCK-8 assays (Fig. 9F), while also inducing robust apoptosis as determined by flow cytometry (Fig. 9G, H). These findings suggest that pharmacologic inhibition of MAT2A suppresses glycolysis and promotes apoptosis in OS cells.

To validate these findings in vivo, we established subcutaneous xenograft models using MNNG/HOS cells and treated tumor-bearing mice with different doses of FIDAS-5. Tumor growth was significantly inhibited in a dose-dependent fashion, with the highest efficacy observed at 20 mg/kg (Fig. 9I–K), while no significant changes in body weight were observed among groups (Fig. 9L). Western blot analysis of tumor tissues confirmed that FIDAS-5 treatment led to a marked reduction in MAT2A, SRF, and PARN expression, accompanied by suppression of PI3K/AKT activation (Fig. 9M). Immunohistochemical staining further demonstrated a consistent decline in MAT2A, PARN, and the proliferation marker Ki-67 across increasing FIDAS-5 doses (Fig. 9N).

Collectively, these results indicate that pharmacological inhibition of MAT2A by FIDAS-5 effectively disrupts the MAT2A–SRF–PARN signaling axis, attenuates glycolytic metabolism, and suppresses osteosarcoma cell proliferation both in vitro and in vivo. Consistent with our findings, pharmacological inhibition of MAT2A with FIDAS-5 has been reported to reduce MAT2A expression, suppress glycolytic metabolism, and impair tumor growth both in vitro and in vivo in multiple myeloma and osteosarcoma models[17,18]. These findings further substantiate the reliability and translational relevance of our inhibitor-based results.

Discussion

OS is the most common primary bone malignancy and the leading cancer affecting adolescents. Despite improvements in multimodal therapy, the prognosis for patients with metastatic, relapsed, or drug-resistant OS remains unsatisfactory, underscoring the urgent need for new targeted therapeutic strategies. Targeted therapies, with their high specificity and reduced toxicity, hold great promise; however, clinically effective molecular targets for OS remain scarce.

In this study, we revealed that MAT2A exerts noncanonical functions beyond its classical role as a SAM-synthetic enzyme. MAT2A directly interacts with SRF and enhances its SUMOylation and nuclear retention, thereby stabilizing SRF and augmenting its transcriptional activity toward *PARN*. This finding suggests that MAT2A functions not only as a metabolic enzyme but also as a signal-modulating scaffold that influences oncogenic

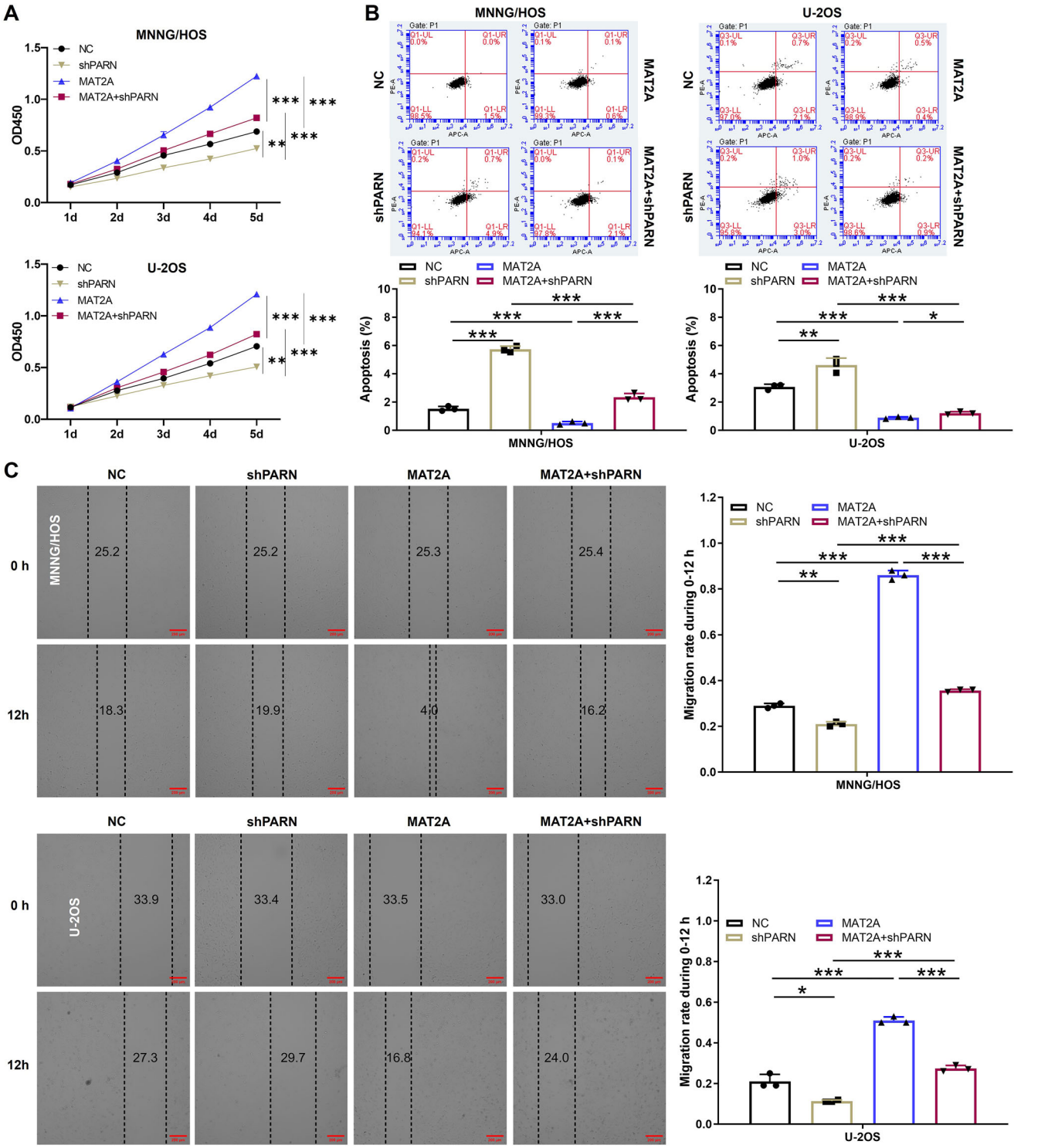

Fig. 6 | MAT2A participated in the regulation of OS cells through PARN. A CCK-8 assay showing that MAT2A overexpression significantly promoted proliferation of MNNG/HOS and U-2OS cells, whereas PARN silencing markedly suppressed cell growth. Co-transfection of MAT2A with shPARN largely abolished the proliferative advantage induced by MAT2A overexpression. **B** Flow cytometric analysis of apoptosis in the indicated groups (NC, shPARN, MAT2A, MAT2A + shPARN). MAT2A overexpression markedly reduced apoptosis, while PARN knockdown increased apoptosis; combined MAT2A + shPARN treatment restored apoptosis to control levels. Quantitative data are shown in the lower panels. **C** Wound-healing assay showing that MAT2A overexpression enhanced, while PARN knockdown inhibited, cell migration in both MNNG/HOS and U-2OS cells. Co-silencing of PARN abrogated the promigratory effect of MAT2A. Images were captured at 0 h and 12 h (scale bar = 200 μm). Migration rates were quantified and plotted on the right. Data are presented as mean ± SD from three independent experiments. $^{*}P < 0.05$, $^{**}P < 0.01$, $^{**}P < 0.001$.

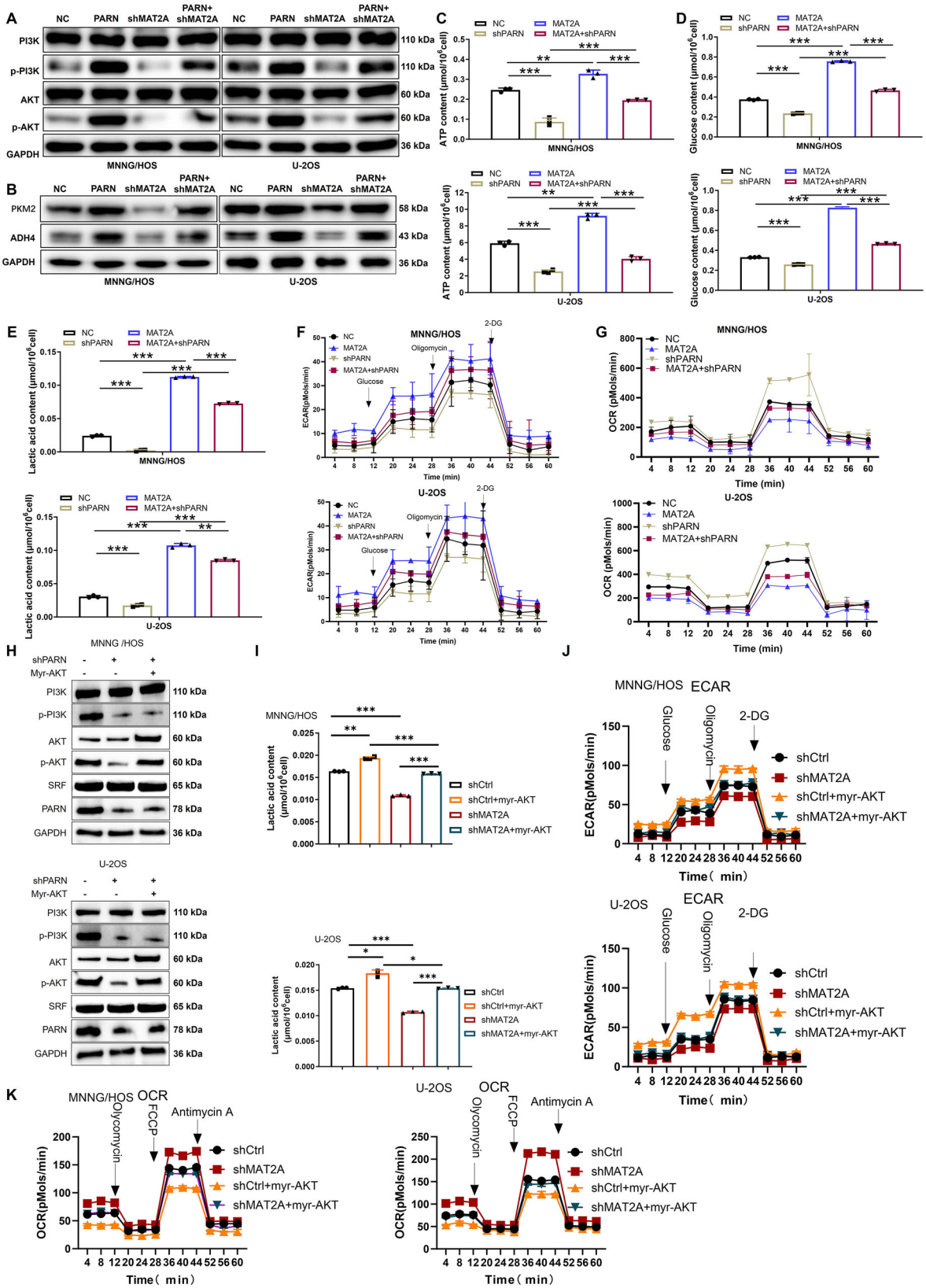

transcriptional programs. Although the precise mechanism through which MAT2A promotes SRF SUMOylation remains unresolved, MAT2A may act as a molecular adaptor bridging SRF with SUMO-conjugating enzymes such as UBC9—an intriguing hypothesis that warrants further investigation.

MAT2A has drawn considerable attention in recent years and is now recognized as a promising therapeutic target. Several MAT2A inhibitors have been identified, and three have progressed into clinical trials for the treatment of MTAP-deficient solid tumors or lymphomas[25]. In OS, we demonstrated that MAT2A is consistently upregulated at tissue, cellular,

Fig. 7 | PARN overexpression rescues PI3K/AKT signaling and glycolytic activity suppressed by MAT2A knockdown in OS cells. A Western blot analysis of PI3K/AKT signaling in MNNG/HOS and U-2OS cells showing that MAT2A knockdown reduced phosphorylation of PI3K and AKT, while PARN overexpression restored p-PI3K and p-AKT levels. GAPDH served as loading control. **B** Western blot analysis showing that knockdown of MAT2A decreased expression of glycolytic enzymes PKM2 and LDHA, whereas PARN overexpression rescued their expression. β-Actin served as loading control. **C**–**E** Quantitative analysis of glycolytic metabolites in the indicated groups (NC, PARN, shMAT2A, PARN + shMAT2A). **C** ATP content, (**D**) glucose consumption, and (**E**) lactate production were all reduced upon MAT2A knockdown but restored by PARN overexpression in both MNNG/HOS and U-2OS cells. **F** Seahorse ECAR analysis showing that MAT2A knockdown suppressed glycolytic flux, whereas PARN overexpression rescued glycolytic activity. **G** OCR analysis showing that PARN overexpression reversed the increase in mitochondrial respiration caused by MAT2A knockdown, indicating metabolic reprogramming compensation. **H** Western blot analysis showing that constitutively active myr-AKT restored p-AKT, SRF, and PARN expression in shPARN cells, confirming that PI3K/AKT activation functions downstream of MAT2A–PARN signaling. GAPDH was used as loading control. **I** Measurement of lactate levels showing that AKT activation by myr-AKT rescued the reduction of lactate production induced by MAT2A knockdown. **J**, **K** Seahorse analyses showing that myr-AKT restored glycolytic flux (ECAR, **J**) and mitochondrial respiration (OCR, **K**) suppressed by MAT2A depletion. Sequential injections of glucose, oligomycin, 2-DG (for ECAR) or FCCP and antimycin A (for OCR) were performed at the indicated time points. Data are presented as mean ± SD from three independent experiments. $^{*}P < 0.05$, $^{**}P < 0.01$, $^{**}P < 0.001$.

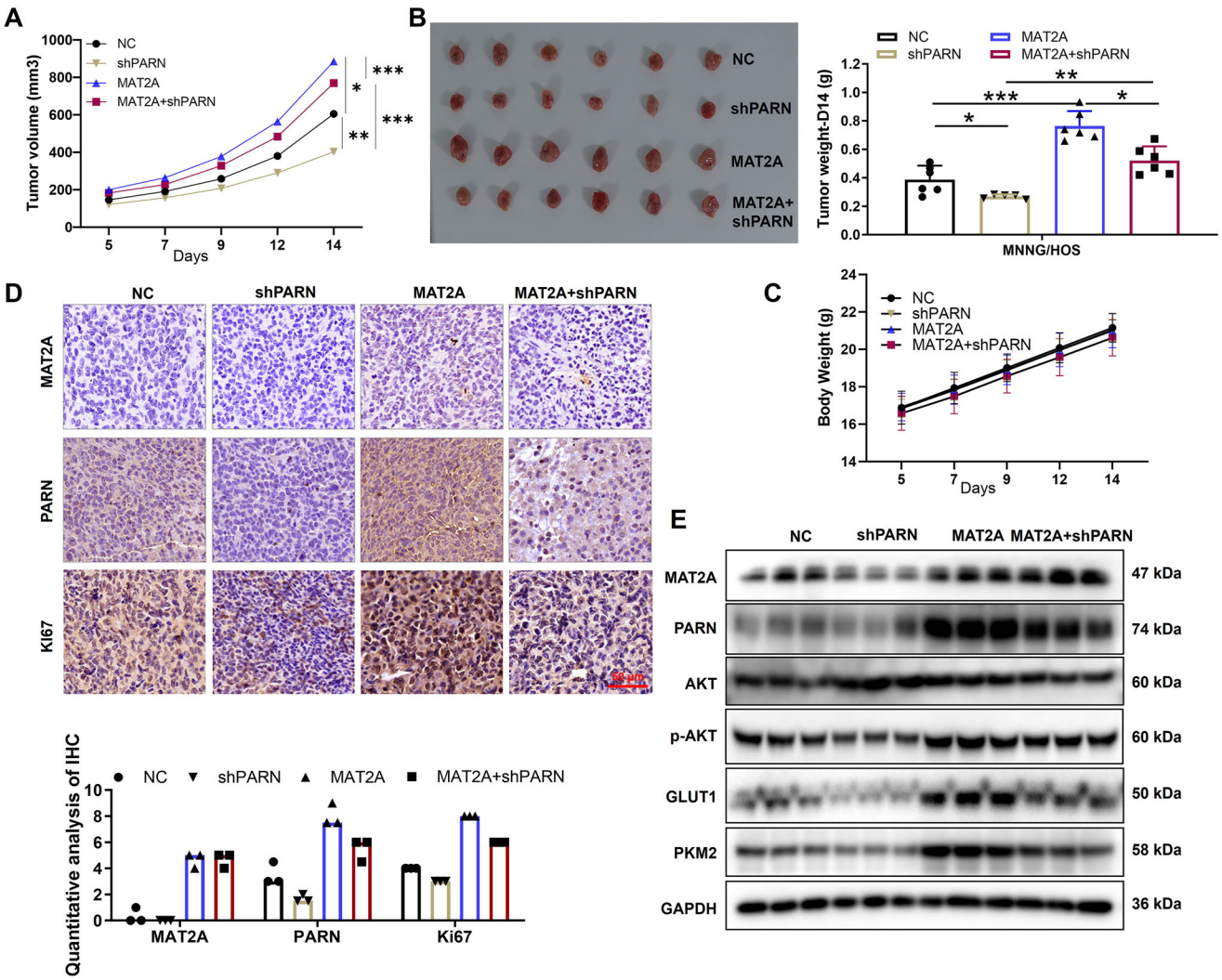

Fig. 8 | In vivo validation of MAT2A-driven aerobic glycolysis regulates OS progression through PARN. A Tumor growth curves of MNNG/HOS xenografts in nude mice injected with the indicated cells (NC, shPARN, MAT2A, MAT2A + shPARN). MAT2A overexpression significantly promoted tumor growth, whereas *PARN* silencing markedly inhibited tumor expansion and abolished the pro-tumorigenic effect of MAT2A. **B** Representative images of excised xenograft tumors and quantitative analysis of tumor weight on day 14 post-inoculation ($n = 6$ per group). MAT2A-overexpressing tumors were larger and heavier, while co-knockdown of PARN significantly reduced tumor mass. **C** Body weight changes of mice during the 14-day observation period, showing no significant difference among groups. **D** Representative immunohistochemical (IHC) staining of MAT2A, PARN, and Ki-67 in xenograft tumor tissues (scale bar = 50 μm). Quantitative IHC analysis revealed increased MAT2A, PARN, and Ki-67 expression in MAT2A-overexpressing tumors, while PARN knockdown reduced these levels. **E** Western blot analysis of tumor tissue lysates showing that MAT2A overexpression enhanced phosphorylation of AKT and increased expression of glycolytic enzymes (GLUT1, PKM2, ADH4), whereas PARN silencing reversed these effects. GAPDH served as loading control. Data are presented as mean ± SD from three independent experiments. $^{*}P < 0.05$, $^{**}P < 0.01$, $^{**}P < 0.001$.

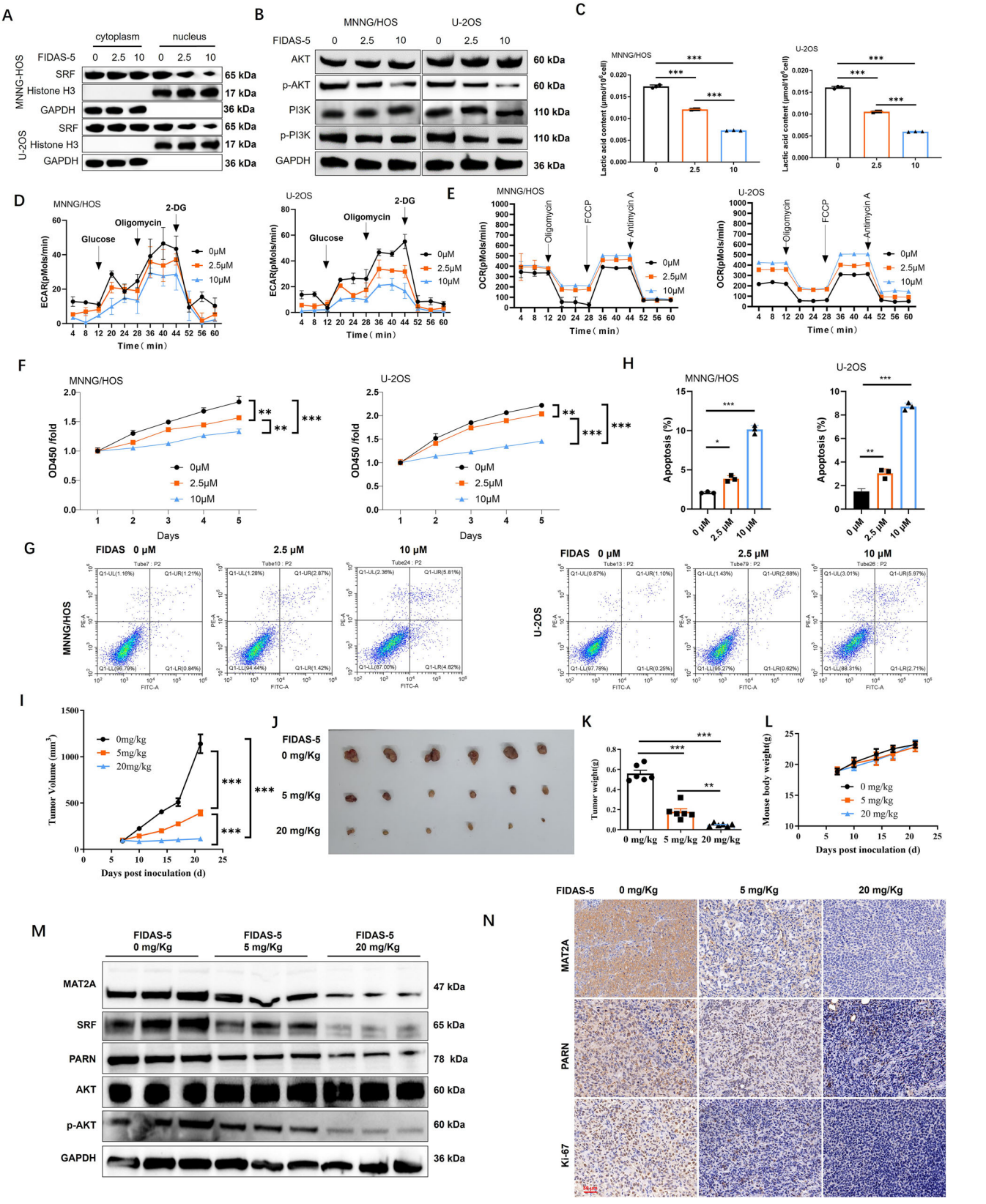

and molecular levels. Loss-of-function studies showed that MAT2A knockdown markedly impaired the proliferative and tumorigenic capabilities of OS cells, establishing MAT2A as a functional driver of OS malignancy. Moreover, tissue microarray analysis revealed a significant association between high MAT2A expression and advanced tumor stage as well as lymphatic metastasis, indicating that MAT2A upregulation accompanies aggressive disease. Larger patient cohorts with survival data will be needed to further define its prognostic significance.

Mechanistically, microarray analysis identified *PARN* as a downstream effector of *MAT2A*. *PARN* downregulation following *MAT2A* knockdown,

Fig. 9 | Pharmacological inhibition of MAT2A suppresses PI3K/AKT signaling, glycolysis, and tumor growth in osteosarcoma. **A** Western blot analysis of cytoplasmic and nuclear fractions showing that the MAT2A inhibitor FIDAS-5 (2.5–10 μM) decreased nuclear SRF levels in MNNG/HOS and U-2OS cells, while total cytoplasmic SRF remained largely unchanged. GAPDH and histone H3 were used as cytoplasmic and nuclear markers, respectively. **B** Western blot analysis showing that FIDAS-5 treatment reduced phosphorylation of PI3K and AKT in a dose-dependent manner, while total PI3K and AKT levels remained unchanged. GAPDH served as loading control. **C** Quantification of lactate content showing that FIDAS-5 significantly decreased lactate production in a dose-dependent manner, indicating inhibition of glycolytic activity. **D** Seahorse ECAR showing that FIDAS-5 suppressed glycolytic capacity in a concentration-dependent manner. **E** OCR analysis showing increased mitochondrial respiration after FIDAS-5 treatment, suggesting a metabolic shift from glycolysis toward oxidative phosphorylation. **F** CCK-8 assay showing that FIDAS-5 treatment inhibited proliferation of MNNG/HOS and U-2OS cells in a dose- and time-dependent manner. **G**, **H** Flow cytometric analysis of apoptosis in MNNG/HOS and U-2OS cells treated with 0, 2.5, or 10 μM FIDAS-5 for 48 h. Quantitative results (**H**) indicate a significant increase in apoptosis following FIDAS-5 exposure. **I** Tumor growth curves of MNNG/HOS xenografts in nude mice treated with vehicle or FIDAS-5 (5 or 20 mg/kg, intraperitoneally, once every two days for 21 days). FIDAS-5 markedly suppressed tumor growth in a dose-dependent manner. **J**, **K** Representative images of excised xenograft tumors and quantitative analysis of tumor weights at day 21, showing significant inhibition of tumor burden by FIDAS-5. **L** Mouse body weights during treatment, showing no significant changes among groups, indicating good tolerability of FIDAS-5. **M** Western blot analysis of tumor tissues showing that FIDAS-5 treatment decreased MAT2A, SRF, PARN, and p-AKT protein levels, without affecting total AKT, confirming that FIDAS-5 suppresses MAT2A–SRF–PARN–AKT signaling in vivo. GAPDH served as loading control. **N** Representative IHC staining of MAT2A, PARN, and Ki-67 in xenograft tumors (scale bar = 50 μm), showing that FIDAS-5 treatment reduced their expression in a dose-dependent manner. Data are presented as mean ± SD from three independent experiments. $^{*}P < 0.05$, $^{**}P < 0.01$, $^{**}P < 0.001$.

together with their positive expression correlation, strongly supports this regulatory relationship. PARN is the major mammalian deadenylase and the only enzyme capable of simultaneously binding the 5′ cap and 3′ poly(A) tail, playing essential roles in nonsense-mediated decay and cytoplasmic polyadenylation[26–28]. Therefore, PARN is considered an important regulator of gene expression[29]. Recent evidence indicates that PARN plays critical roles in embryogenesis, oocyte maturation, cell cycle progression, telomere maintenance, non-coding RNA maturation, and ribosome biogenesis[30]. Pathogenic variants of the PARN gene have also been identified in various cancers[29,31]. Here, we demonstrated that SRF binds directly to the *PARN* promoter and that MAT2A enhances this transcriptional interaction, thereby activating *PARN* expression. Functionally, PARN knockdown partially reversed the pro-tumorigenic effects of MAT2A overexpression, confirming that MAT2A regulates OS progression through the SRF–PARN axis. Furthermore, the catalytically inactive MAT2A-D180A mutant retained the ability to promote SRF nuclear localization and *PARN* transcription, revealing a SAM-independent, non-enzymatic mechanism of action—an emerging paradigm for metabolic enzymes[32–35].

Given that the PI3K/AKT signaling pathway is one of the most important oncogenic cascades in human cancers[36], and its activation has been shown to enhance aerobic glycolysis and accelerate OS progression[19], we examined whether MAT2A influences this pathway. Our findings revealed that MAT2A regulates PI3K/AKT signaling through PARN and modulates multiple aspects of aerobic glycolysis, including glucose uptake, lactate production, ATP generation, ECAR, and OCR. Since aerobic glycolysis represents a hallmark of metabolic reprogramming that sustains tumor growth[37], these results highlight a previously unrecognized metabolic role of MAT2A in OS.

Importantly, pharmacological inhibition of MAT2A using FIDAS-5 significantly suppressed OS cell proliferation, glycolytic activity, and tumor growth in vitro and in vivo. FIDAS-5, known to augment bortezomib-based therapy in multiple myeloma, also exhibited potent antitumor efficacy in OS by disrupting the MAT2A–SRF–PARN axis and inhibiting PI3K/AKT activation[17,18]. These results demonstrate the translational potential of MAT2A inhibition and support its broader applicability across multiple malignancies.

Together, our findings reveal that MAT2A orchestrates osteosarcoma progression through a SAM-independent, post-translational mechanism that stabilizes SRF and activates the PARN–PI3K/AKT–glycolysis axis. Targeting this signaling cascade—either genetically or pharmacologically-represents a promising therapeutic avenue for osteosarcoma management.

Methods

Bioinformatics analysis

scRNA-seq data from GSE162454 and GSE169396 were processed using the anchor-based integration method to correct batch effects. Principal component analysis (PCA) was performed for dimensionality reduction, followed by Uniform Manifold Approximation and Projection (UMAP) for clustering and visualization. Cell types were annotated based on canonical marker genes, and differential gene expression analysis was conducted. The results were visualized using dot plots, volcano plots, and heatmaps.

IHC analysis

This study was approved by the Institutional Committee of Nanfang Hospital, Southern Medical University, and all patients were fully informed and provided written informed consent before surgery. Tumor tissue and normal tissue of 71 patients with OS were collected and made into tissue microarray for immunohistochemistry. According to the protocol provided in the literature, the tissue microarray was subjected to IHC staining[38]. The primary and secondary antibodies used in this experiment were listed in Supplementary Table 3.

Cell culture

Human osteoblast hfOB 1.19 (RRID: CVCL_3708) and OS cell lines MNNG/HOS (RRID: CVCL_0439), U-2OS (RRID: CVCL_0042) and KHOS-240S (RRID: CVCL_2544) were obtained from the Bena Technology (Hangzhou, China). hfOB 1.19 and MNNG/HOS was maintained in 90% DMEM-H with 10% FBS additive (Gibco, USA). U-2OS and KHOS-24OS cells were cultured in 90% RPMI-1640 containing 10% FBS. All cells were maintained in an incubator at 37 °C with 5% CO_2. MNNG/HOS and U-2OS cell lines have been authenticated using STR profiling within the last three years has been included in Supplementary material.

RNA extraction and qRT-PCR

Total RNA was extracted by TRIzol reagent (Invitrogen) and the quality of total RNA was assessed by a Nanodrop 2000 spectrometer (Thermo Fisher Scientific). According to the manufacturer's instructions, total RNA was reverse-transcribed into cDNA with Promega M-MLV. On the platform of Sequence Detection System (TAKARA), cDNA was added to the reaction system using SYBR Green master mix Kit (TAKARA) for real-time PCR. Using *GAPDH* as control, the relative quantitative analysis of gene expression was performed by $2^{-\Delta\Delta Ct}$. The relevant primers are shown in Supplementary Table 4.

Western blotting assay (WB) and Co-IP

The experiment was performed as described previously[39]. The cells are cleaved in a lysate buffer and protease inhibitor mixture (Sigma). For Co-IP, cell lysate was prepared for WB assay, and 1.0–1.2 mg proteins were incubated with normal rabbit IgG (as control) for 2 h, and followed by 2 h incubation with 20 μL protein A/G-beads. The cleared protein antibody beads complex was incubated at 100 °C for 10 min. Then the proteins in the immunocomplex were separated by 10% SDS-PAGE as WB assay, and used for immunoblotting to identify interacting proteins. The corresponding antibodies are shown in Supplementary Table 3.

Plasmid construction, lentivirus infection, and transfection

The small-hairpin RNA (shRNA) sequences targeting *MAT2A* (named as shMAT2A; shMAT2A-1: 5'-GCTGTTAAACACATTGGATAT-3'; shMAT2A-2: 5'-CCAGATAAGATTTGTGACCAA-3'; shMAT2A-3: 5'-TGCGAAATACCTTGATGAGGA-3'), targeting *PARN* (named as shPARN; shPARN-1: 5'-TATGACACAGCCTCTGAACAA-3'; shPARN-2: 5'-TGGATACTAAATTGATGGCCA-3'; shPARN-3: 5'-CAACACATCCCTTGCGGAATT-3'), and the scramble control (shCtrl: 5'-TTCTCCGAACGTGTCACGT-3') were cloned into the LV-006 lentiviral vector using T4 DNA ligase.

For gain-of-function studies, full-length *MAT2A* and *PARN* coding sequences were inserted into the BR-V-108 lentiviral expression vector. For *MAT2A* truncation analysis, three deletion constructs were generated: MAT2A-Δ1 (Δaa 2–70), MAT2A-Δ2 (Δaa 71–330), and MAT2A-Δ3 (Δaa 331–395). Each fragment was amplified by PCR with primers flanking the indicated regions, followed by ligation into BR-V-108. All constructs were verified by Sanger sequencing.

To generate the catalytically inactive *MAT2A* mutant, site-directed mutagenesis was performed to substitute the conserved aspartate at position 180 with alanine (D180A). Mutagenesis was conducted using a standard PCR-based overlap extension method with mutation-specific primers, followed by DpnI digestion to remove the methylated parental plasmid. The resulting MAT2A-D180A mutant was cloned into BR-V-108 and validated by Sanger sequencing to confirm the presence of the intended point mutation and the absence of off-target changes.

Lentiviral particles encoding full-length *MAT2A*, *MAT2A* truncation mutants, MAT2A-D180A, or PARN were produced and transduced into MNNG/HOS and U-2OS cells at ~80% confluence using Lipofectamine 3000 (Thermo Fisher Scientific). Stable cell lines were selected with puromycin (2 μg/mL) for ≥7 days before subsequent assays.

Cell Counting Kit-8 (CCK-8) assay

Cell proliferation was assessed using the Cell Counting Kit-8 (CCK-8; Dojindo, Japan). Briefly, osteosarcoma cells were seeded into 96-well plates at a density of 1×10^4 cells/well in 100 μL complete medium and allowed to adhere overnight. At the indicated time points (0, 24, 48, 72, and 96 h), 10 μL of CCK-8 solution was added to each well and incubated for 2 h at 37 °C. Absorbance at 450 nm was measured using a microplate reader (BioTek). The proliferation rate was calculated based on optical density (OD) values.

Celigo cell-counting assay

Cell proliferation was further evaluated using a Celigo image cytometer (Nexcelom Bioscience). Briefly, cells were seeded into 96-well plates at a density of 500–1000 cells/well and cultured under standard conditions. Plates were scanned daily for 5 consecutive days using the Celigo system. The number of viable cells was automatically identified and counted based on fluorescence or bright-field images according to the manufacturer's algorithm. Growth curves were generated from the normalized cell counts to reflect proliferation kinetics.

Annexin V-APC (FITC)/PI apoptosis assay

Cell apoptosis was evaluated using an Annexin V-APC (FITC)/PI Apoptosis Detection Kit (eBioscience or equivalent) following the manufacturer's protocol. Briefly, osteosarcoma cells with or without lentiviral infection (virus carrying GFP fluorescence) were harvested, washed twice with cold PBS, and resuspended in 1× binding buffer at a concentration of 1×10^6 cells/mL. Subsequently, 5 μL Annexin V-APC (FITC) and 5 μL propidium iodide (PI) were added to 100 μL of the cell suspension and incubated for 15 min at room temperature in the dark. After adding 400 μL binding buffer, samples were analyzed on a flow cytometer (BD FACSCanto II). Early apoptotic (Annexin V-APC $(FITC)^+/PI^-$) and late apoptotic (Annexin V-APC $(FITC)^+/PI^+$) populations were quantified (Supplementary Fig. 4).

PI single-staining apoptosis assay

To confirm apoptosis independently of GFP-related fluorescence interference, PI single-staining was performed. Cells were harvested, washed twice with ice-cold PBS, and fixed in 70% ethanol at 4 °C overnight. After washing with PBS, cells were incubated with PI/RNase staining buffer (BD Biosciences) for 30 min at room temperature in the dark. PI fluorescence was recorded using the PE-TEXAS Red or PE-TM channel, avoiding FITC or GFP channels. The percentage of PI-positive apoptotic cells was quantified.

All samples were analyzed using FlowJo (Tree Star, version X). Cellular debris and doublets were excluded using FSC/SSC and pulse-geometry gating. A minimum of 10,000 events per sample was acquired. Apoptosis was reported as the sum of early and late apoptotic cells.

Wound-healing assay

Briefly, cells (5×10^4 cells/well) were seeded onto a 96-well dish. Scratches crossing the cell monolayer were made by a 96-wounding replicator (VP scientific, USA) while cell confluence reached over 90%. After rinsing gently with serum-free medium for 2−3 times, medium with 0.5% FBS was added and cultured for several hours and photographs were taken by a fluorescence microscope at indicated timepoints and migration rate was calculated.

Transwell assay

Transwell assay was performed by Corning Transwell Kit (Corning, USA). First, cells were collected, trypsinized, counted, and incubated in the upper chamber with 100 μL medium without FBS in a 24-well plate (5×10^4 cells/well). Six hundred microliters of medium supplemented with 30% FBS was added in the lower chamber. After 16 or 24 h incubation for MNNG/HOS or U-2OS at 37 °C with 5% CO_2, nonmetastatic cells were removed with a cotton swab. Four hundred microliters of Giemsa were added for staining and the migratory ability of cells was analyzed.

GeneChip microarray

Affymetrix human GeneChip PrimeView combined with Affymetrix Scanner 3000 was performed to elaborate the molecular mechanism, and the outcomes were followed by the manufacturer. Accordingly, the volcano plot and hierarchical clustering of the shCtrl and *MAT2A* OS cells were presented by the differentially expressed genes (DEGs) with criterion of $|\text{Fold Change}| \geq 1.3$ and false discovery rate (FDR) < 0.05.

Glycolysis assay

Cells were seeded into 96-well plates (2000 cells/well) and further cultured in MEM (10% FBS) at 37 °C with 5% CO_2. The contents of ATP, glucose and lactic acid were evaluated according to the instructions of the assay kit (Beijing Solarbio Science & Technology Co., Ltd). OCR and ECAR were measured using XFe96 Extracellular Flux Analyzer (Agilent) and BCA (Pierce) according to manufacturer's instructions.

Xenograft tumor model

Inclusion and exclusion criteria: no animals or experimental units were excluded from the study unless they met pre-defined humane endpoint criteria (e.g., ulceration, impaired mobility, or tumor burden exceeding institutional limits). These criteria were established a priori in accordance with institutional animal welfare guidelines. All animals that survived to the planned experimental endpoint were included in the final analysis. No data points were excluded during statistical analysis unless technical failure occurred (e.g., incomplete tissue collection or instrument malfunction), and no exclusion was made based on experimental outcomes.

For two-group (shCtrl, shMAT2A; $n = 5$) and inhibitor treatment experiments (Vehicle, FIDAS-5 5 mg per Kg and 20 mg per Kg; $n = 6$), pathogen-free male BALB/c nude mice (4–5 weeks old, 18–22 g; Vitalriver Experimental Animal Technology Co., Ltd., Beijing, China) were used. For four-group rescue experiments (NC, PARN, shMAT2A, PARN+shMAT2A; $n = 6$), male NCG immunodeficient mice (4−5 weeks old; GemPharmatech, China) were used. All animals were maintained under specific pathogen-free (SPF) conditions (20−25 °C, 50–60% humidity, 12 h light/dark cycle) with ad

libitum access to food and water. All procedures were approved by the Animal Care and Use Ethics Committee of Southern Medical University and performed in accordance with institutional guidelines.

Random allocation was applied to assign animals to experimental groups. Group assignment was performed using a simple random draw procedure to ensure unbiased allocation. No stratification or blocking methods were used.

For xenograft establishment, 1×10^7 MNNG/HOS cells suspended in PBS were subcutaneously injected into the right flank of each mouse. For inhibitor studies, mice received FIDAS-5 or vehicle control according to the dosing schedule described in the Results section. Tumor length (L) and width (W) were measured every 2–3 days using digital calipers, and tumor volume was calculated as $\pi/6 \times L \times W^2$. Body weight was recorded throughout the experiment to assess potential systemic toxicity.

FIDAS-5 treatment: For inhibitor studies, mice received FIDAS-5 at 20 mg/kg via intraperitoneal injection once daily (QD) beginning on day 5 post-implantation, when tumors became palpable. Control mice received vehicle.

At the endpoint, mice were euthanized by cervical dislocation. Tumors were excised, photographed, weighed, and processed for immunohistochemistry or Western blot analysis.

Dual-luciferase reporter assay

To assess SRF-dependent transcriptional activation of PARN, the wild-type PARN promoter (*PARN*-WT) was cloned upstream of the firefly luciferase gene. The predicted SRF-binding motif within this region is a GC-rich sequence (5'-GCCCCGCCCCCGCCGCCGCGCA-3'). A mutant promoter (*PARN*-MUT) was generated by replacing this motif with an AT-rich, non-homologous sequence (5'-TAAGATGGAAGTAGTGATATAC-3') to disrupt SRF binding while preserving promoter length.

Cells were seeded in 24-well plates and co-transfected with PARN-WT or PARN-MUT reporter plasmids together with a Renilla luciferase plasmid as an internal control, using Lipofectamine 3000 (Thermo Fisher Scientific). Where indicated, SRF, MAT2A, or shRNA constructs were co-transfected. After 48 h, firefly and Renilla luciferase activities were measured using the Dual-Luciferase Reporter Assay System (Promega), and firefly signals were normalized to Renilla signals to determine relative promoter activity.

ChIP-qPCR

ChIP was carried out by following the protocol of SimpleChIP® Enzymatic Chromatin IP Kit (CST, USA). Briefly, the cells are cross-linked with 1% formaldehyde, lysed and ultrasound treated to produce chromatin fragments of 200−1000 bp, which are immunoprecipitated with IgG or SRF antibodies. Immunoprecipitated DNA was analyzed by qRT-PCR. Information for antibodies and primers are listed in Supplementary Tables 3 and 4, respectively.

Statistics and Reproducibility

All statistical analyses were performed using GraphPad Prism 9.0 (GraphPad Software). Data are presented as mean ± standard deviation (SD) unless otherwise specified. For comparisons between two groups, unpaired two-tailed Student's t-tests were applied. For experiments involving more than two groups, one-way analysis of variance (ANOVA) followed by Tukey's post-hoc test was used. Tumor growth curves were analyzed using two-way ANOVA with repeated measures. The significance threshold was set at $P < 0.05$.

All experiments were independently repeated three times with similar results. For in vivo studies, sample sizes were determined based on commonly accepted standards in the field and were sufficient to detect biologically meaningful differences. Animals were randomly assigned to experimental groups, and investigators were blinded to group allocation during tumor size measurements and data analysis whenever feasible. No data were excluded unless pre-established humane endpoints were reached.

Inclusion & Ethics

This study was conducted in strict accordance with institutional ethical guidelines and national regulations. All animal experiments complied with the guidelines of the Animal Care and Use Ethics Committee of Nanfang Hospital, Southern Medical University and followed standard ARRIVE reporting principles (Approval No. NFYY-2022-0376). No human or animal subjects were excluded on the basis of sex, race, ethnicity, or socioeconomic status. Experimental groups were assigned without bias, and analyses were performed under blinded conditions whenever feasible. All efforts were made to minimize animal suffering and to use the minimum number of animals required to achieve statistical rigor.

Data availability

The TCGA datasets analyzed in this study are publicly available from the Genomic Data Commons (https://portal.gdc.cancer.gov/). Additional datasets used for bioinformatic analyses are available from GEO under accession numbers indicated in the Methods section. All other data supporting the findings of this study, including raw Western blots, flow cytometry files, and numerical values underlying the graphs, are provided within the manuscript and its Supplementary Information. Uncropped and unprocessed Western blot and gel images have been included in Supplementary Fig. 5. The numerical source data underlying all figures presented in the manuscript are provided in the Supplementary Data file. Source data are available from the corresponding author upon reasonable request.

Received: 7 March 2025; Accepted: 5 January 2026;
Published online: 13 January 2026

References

1. Prater, S. & McKeon, B. in *StatPearls* (StatPearls Publishing Copyright © 2024, StatPearls Publishing LLC., 2024).
2. Du, X. et al. Molecular mechanisms of osteosarcoma metastasis and possible treatment opportunities. *Front. Oncol.* **13**, 1117867 (2023).
3. Xu, Y. et al. Twenty-year outcome of prevalence, incidence, mortality and survival rate in patients with malignant bone tumors. *Int. J. Cancer* **154**, 226–240 (2024).
4. Li, S., Zhang, H., Liu, J. & Shang, G. Targeted therapy for osteosarcoma: a review. *J. Cancer Res. Clin. Oncol.* **149**, 6785–6797 (2023).
5. Wang, S. et al. The Targeted Therapies for Osteosarcoma via Six Major Pathways. *Curr. Mol. Pharmacol.* **17**, e210823220109 (2024).
6. Kotb, M. et al. Consensus nomenclature for the mammalian methionine adenosyltransferase genes and gene products. *Trends Genet* **13**, 51–52 (1997).
7. Lu, S. C. & Mato, J. M. Role of methionine adenosyltransferase and S-adenosylmethionine in alcohol-associated liver cancer. *Alcohol* **35**, 227–234 (2005).
8. Bottiglieri, T. S-Adenosyl-L-methionine (SAMe): from the bench to the bedside-molecular basis of a pleiotrophic molecule. *Am. J. Clin. Nutr.* **76**, 1151S–1157S (2002).
9. Timp, W. & Feinberg, A. P. Cancer as a dysregulated epigenome allowing cellular growth advantage at the expense of the host. *Nat. Rev. Cancer* **13**, 497–510 (2013).
10. Cai, J., Sun, W. M., Hwang, J. J., Stain, S. C. & Lu, S. C. Changes in S-adenosylmethionine synthetase in human liver cancer: molecular characterization and significance. *Hepatology* **24**, 1090–1097 (1996).
11. Simile, M. M. et al. MicroRNA-203 impacts on the growth, aggressiveness and prognosis of hepatocellular carcinoma by targeting MAT2A and MAT2B genes. *Oncotarget* **10**, 2835–2854 (2019).
12. Xu, J., Wu, D., Wang, S. & Wang, Z. MAT2B expression correlates with poor prognosis in triple-negative breast cancer. *Cancer Manag Res* **11**, 5501–5511 (2019).
13. Zhang, Y. et al. Activation of MAT2A-RIP1 signaling axis reprograms monocytes in gastric cancer. *J. Immunother. Cancer* **9**, https://doi.org/10.1136/jitc-2020-001364(2021).
14. Chen, Y. W. et al. Circ_0044516 Regulates miR-136/MAT2A Pathway to Facilitate Lung Cancer Development. *J. Immunol. Res* **2021**, 5510869 (2021).

15. Wang, L. et al. SYVN1-MTR4-MAT2A Signaling Axis Regulates Methionine Metabolism in Glioma Cells. *Front Cell Dev. Biol.* **9**, 633259 (2021).
16. Yang, C. et al. Methionine orchestrates the metabolism vulnerability in cisplatin resistant bladder cancer microenvironment. *Cell Death Dis.* **14**, 525 (2023).
17. Wang, Y. et al. S-adenosylmethionine biosynthesis is a targetable metabolic vulnerability in multiple myeloma. *Haematologica* **109**, 256–271 (2024).
18. Xia, S., Liang, Y., Shen, Y., Zhong, W. & Ma, Y. MAT2A inhibits the ferroptosis in osteosarcoma progression regulated by miR-26b-5p. *J. Bone Oncol.* **41**, 100490 (2023).
19. Deng, B., Deng, J., Yi, X., Zou, Y. & Li, C. ROCK2 Promotes Osteosarcoma Growth and Glycolysis by Up-Regulating HKII via Phospho-PI3K/AKT Signalling. *Cancer Manag. Res.* **13**, 449–462 (2021).
20. Wang, J. & Schwartz, R. J. Sumoylation and regulation of cardiac gene expression. *Circ. Res* **107**, 19–29 (2010).
21. Patyal, P. et al. Rho/SRF Inhibitor Modulates Mitochondrial Functions. *Int. J. Mol. Sci.* **23**, https://doi.org/10.3390/ijms231911536 (2022).
22. Li, J. et al. Signalosome-Regulated Serum Response Factor Phosphorylation Determining Myocyte Growth in Width Versus Length as a Therapeutic Target for Heart Failure. *Circulation* **142**, 2138–2154 (2020).
23. Li, K. et al. The SUMOylation and ubiquitination crosstalk in cancer. *J. Cancer Res Clin. Oncol.* **149**, 16123–16146 (2023).
24. Han, Z. J., Feng, Y. H., Gu, B. H., Li, Y. M. & Chen, H. The post-translational modification, SUMOylation, and cancer (Review). *Int J. Oncol.* **52**, 1081–1094 (2018).
25. Li, C. et al. Overview of Methionine Adenosyltransferase 2A (MAT2A) as an Anticancer Target: Structure, Function, and Inhibitors. *J. Medicinal Chem.* **65**, 9531–9547 (2022).
26. Cevher, M. A. et al. Nuclear deadenylation/polyadenylation factors regulate 3' processing in response to DNA damage. *EMBO J.* **29**, 1674–1687 (2010).
27. Devany, E., Zhang, X., Park, J. Y., Tian, B. & Kleiman, F. E. Positive and negative feedback loops in the p53 and mRNA 3' processing pathways. *Proc. Natl. Acad. Sci. USA* **110**, 3351–3356 (2013).
28. Gherzi, R. et al. A KH domain RNA binding protein, KSRP, promotes ARE-directed mRNA turnover by recruiting the degradation machinery. *Mol. Cell* **14**, 571–583 (2004).
29. Zhang, F. W. et al. Poly(A)-specific ribonuclease protein promotes the proliferation, invasion and migration of esophageal cancer cells. *World J. Gastroenterol.* **29**, 4783–4796 (2023).
30. Nanjappa, D. P. et al. Poly (A)-specific ribonuclease (PARN): More than just "mRNA stock clearing. *Life Sci.* **285**, 119953 (2021).
31. Yin, J. et al. Cross-talk between PARN and EGFR-STAT3 Signaling Facilitates Self-Renewal and Proliferation of Glioblastoma Stem Cells. *Cancer Res.* **83**, 3693–3709 (2023).
32. Li, J. T. et al. Dietary folate drives methionine metabolism to promote cancer development by stabilizing MAT IIA. *Signal Transduct. Target Ther.* **7**, 192 (2022).
33. Li, F. et al. Blocking methionine catabolism induces senescence and confers vulnerability to GSK3 inhibition in liver cancer. *Nat. Cancer* **5**, 131–146 (2024).
34. Zhang, S. et al. Design and Structural Optimization of Methionine Adenosyltransferase 2A (MAT2A) Inhibitors with High In Vivo Potency and Oral Bioavailability. *J. Med Chem.* **66**, 4849–4867 (2023).
35. Hung, M. H. et al. Tumor methionine metabolism drives T-cell exhaustion in hepatocellular carcinoma. *Nat. Commun.* **12**, 1455 (2021).
36. Jiang, N. et al. Role of PI3K/AKT pathway in cancer: the framework of malignant behavior. *Mol. Biol. Rep.* **47**, 4587–4629 (2020).
37. Abbaszadeh, Z., Cesmeli, S. & Biray Avci, C. Crucial players in glycolysis: Cancer progress. *Gene* **726**, 144158 (2020).
38. Kamyab-Hesary, K., Ghanadan, A., Balighi, K., Mousavinia, S. F. & Nasimi, M. Immunohistochemical Staining in the Assessment of Melanoma Tumor Thickness. *Pathol. Oncol. Res* **26**, 885–891 (2020).
39. Sule, R., Rivera, G. & Gomes, A. V. Western blotting (immunoblotting): history, theory, uses, protocol and problems. *BioTechniques* **75**, 99–114 (2023).

Acknowledgements

This work was supported by National Natural Science Foundation of China (Approval no.82303252), Guangdong Basic and Applied Basic Research Foundation (Approval no. 2022 A1515012479), President Foundation of The Third Affiliated Hospital of Southern Medical University (Approval no. YM202209, YP202216), the Joint Project of the Medical Science and Technology Research Program of Henan Province (Approval no. LHGJ20210339).Henan Medical Science and Technology Research Program Joint Construction Project (LHGJ20210285).

Author contributions

The subject design was completed by Runguang Li, Yi Shen and Canjun Zeng. The operation of the experiment was carried out by Zhinan Ren, Haoming Chen and Qi Qiao. Data analysis by Zehao Xie and Jianhua Hu finished. The article written by Zhinan Ren completed. The final data review and article review by Runguang Li, Yi Shen and Canjun Zeng.

Competing interests

The authors declare no competing interests.

Additional information

Supplementary information The online version contains supplementary material available at https://doi.org/10.1038/s42003-026-09518-w.

Correspondence and requests for materials should be addressed to Canjun Zeng, Yi Shen or Runguang Li.

Peer review information *Communications Biology* thanks Zhi Shi and the other, anonymous, reviewer(s) for their contribution to the peer review of this work. Primary Handling Editor: Mengtan Xing. A peer review file is available.